J. Mech. Phys. Solids 145 (2020) 104162

Contents lists available at ScienceDirect

Journal of the Mechanics and Physics of Solids

journal homepage: www.elsevier.com/locate/jmps

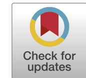

Dual beam-shear differential interference microscopy for full-field surface deformation gradient characterization

Zhuohui Zeng [a], Hoi-Chun Chiu [b], Luwei Zhao [c], Teng Zhao [c], Chenbo Zhang [a,d], Mostafa Karami [a], Hongyu Yu [a], Shengwang Du [b], Xian Chen [*,a]

[a] Department of Mechanical and Aerospace Engineering, Hong Kong University of Science and Technology, Hong Kong
[b] Department of Physics, Hong Kong University of Science and Technology, Hong Kong
[c] Light Innovation Technology Ltd., Hong Kong
[d] HKUST Jockey Club Institute for Advanced Study, Hong Kong University of Science and Technology, Hong Kong

ARTICLE INFO

Keywords:
Dual optical beam-shear differential interference
4D Surface topography
Deformation gradient
Mesomechanics

ABSTRACT

We propose a new experimental mechanics method: dual beam-shear differential interference microscopy (DInM) for full-field surface deformation measurement. The method integrates the principles of differential interference contrast, photoelasticity, digital image correlation and the theories of continuum mechanics for a 4D quantification of the surface topography. Our first DInM prototype provides the lateral resolution of 787nm for up to 12% measurable out-of-plane strains. The resolution can be improved by using the shorter spectrum light and higher magnification objective lens. We use our system to characterize the buckling profile of Si microribbon on an elastomer substrate, which was verified by atomic force microscopy. We also demonstrate the stress-induced phase transformation in NiTi alloy by our system. The evolution of the surface topographies and the full-field deformation gradients are successfully captured and quantified. The dynamic measurement provides the information to calculate the relative transformation strains between phases of different symmetries. The establishment of dual beam-shear DInM opens a new avenue in the field of experimental meso/micromechanics.

1. Introduction

Despite of state-of-art technologies for mechanics characterization in nanometer scale and beyond, the majority of modern mechanics problems need to be studied in the scale from microns to sub-millimeters, such as the buckling of thin shell structures, the deformations of semiconductor devices and biomedical implants under sophisticated loading. A typical paradigm of continuum mechanism is to study the topographical map of a deformable body in $\mathbb{R}^3$. To investigate such a deformation map, we need to know the displacement field of each of the points in current configuration. In fact, it would be better to know the gradient of the displacement field or the gradient of the local deformation, thus the strain field. In continuum scale, the most popular experimental mechanics approach for this purpose is the digital image correlation, which can essentially track the spatial positions of a set of subdomains in reference configuration. A straightforward outcome by maximizing the cross-correlation between undeformed and deformed images is the in-plane displacement field (u, v). The set of gradients

* Corresponding author.
E-mail address: xianchen@ust.hk (X. Chen).

https://doi.org/10.1016/j.jmps.2020.104162
Received 25 April 2020; Received in revised form 8 August 2020; Accepted 20 September 2020
Available online 28 September 2020
0022-5096/© 2020 Elsevier Ltd. All rights reserved.

$$(\partial u/\partial x, \partial u/\partial y, \partial v/\partial x, \partial v/\partial y)$$

are computed by further iterative optimizations under the elastically linear assumption. In tandem with the rapid growth of computer-based analysis algorithms the digital image correlation has become the leading technique for surface deformation measurements in the past few years (Peters and Ranson, 1982; Sutton et al., 1983; 2009), but some limitations still exist. The primary limitation of digital image correlation is its assumption that the gradients ($\partial w/\partial x$, $\partial w/\partial y$) do not influence the in-plane deformation too much where w is the out-of-plane displacement component. With the conventional single camera setting, it is rather difficult to directly characterize the out-of-plane deformation. Particularly, when the out-of-plane distortion is sufficiently large, the errors of deformation gradients given by conventional digital image correlation become not negligible. Here we do not discuss the two-camera settings for 3D digital image correlation because both experimental setting and the post-data processing algorithm are much complicated than the conventional experiment. In addition, the quality and randomness of speckle pattern on the sample surface play important roles in the accuracy and reliability of the measurement. Sometimes it is not easy to observe the evolution of microstructure especially fine surface reliefs due to the coverage of the speckle pattern.

Another branch of experimental mechanics is the interferometry-based approaches such as traditional photoelasticity, Moiré interferometry and holography. With the ordinary optical settings, these methods are suitable to characterize the in-plane components of local deformation gradient. A common feature of these techniques is that the surface deformation field is resolved by periodic fringes. The accuracy of the measurements strongly depends on the environmental stability and the quality of light source. Some even depend on the quality of birefringent coatings or gratings. Among current interferometry-based characterizations, it is nearly impossible to conduct a direct microstructure observation simultaneously with the mechanics measurement.

A new experimental method (Zeng et al., 2019) was proposed recently to quantify the surface reliefs of a phase-transforming crystalline solid, which enables the observation of microstructure and the instantaneous measurement of the spatial configuration of the domain in out-of-plane direction. The key component of this characterization is the differential interference contrast (DInC[1]) technique. In fact, the DInC technique has been widely used in biology to achieve the contrast of transparent sample since 1950s (Nomarski, 1952; Smith, 1952). Since then various mathematical models have been developed to study the relation between the intensity of transmitted light and the phase lag produced by optical path gradient (Shribak and Inoué, 2006). The goal is to optimize the image contrast for unlabeled transparent living cells based on their birefringence property (Nguyen et al., 2017). The principle of DInC can be also used for opaque materials in a reflected setting, with which the surface topography can be fully determined beyond just achieving optimal phase contrast in all orientations. However, up to now, the quantitative information extracted from the differential interference contrast has not been formally integrated to the experimental mechanics because neither mechanics theory nor formal experimental settings are rationalized for the full-field deformation tensor measurement. In this paper, we name this new method (Zeng et al., 2019) differential interference microscopy (DInM) because the phase contrast is no longer our experimental goal. The DInM should be an emerging approach to characterize the mesoscale surface topography in $\mathbb{R}^3$encoded by the map of local deformation gradients. If we consider a surface deformation map $\mathbf{x} : \mathcal{B}_0 \to \mathbb{R}^3$,for any $\mathbf{X} \in \mathcal{B}_0$the DInM is supposed to give a measure of

$$\left(\frac{\partial x_3}{\partial X_1}, \frac{\partial x_3}{\partial X_2}\right) \tag{1}$$

where the indices 1 and 2 denote the in-plane components while the index 3 denotes the out-of-plane component. But the most recent DInM method can only provide the spatial form of only one of the components in the expression (1). The detailed limitations is concluded in Section 2.

2. Review of single beam-shear mode differential interference microscopy

The underlying principle and mathematical framework of the single beam-shear DInM have been introduced in reference Zeng et al. (2019). Fig. 1 compares the DInM (a) and the conventional photoelastic method (b) used for continuum mechanics characterization. Both methods use the birefringent crystal to obtain certain phase lag between orthogonal polarization components. For example, there is a quarter period retardance between p_1 and p_2 polarizations as shown in both (a) and (b) of Fig. 1, but such a retardance plays different roles in different optical setups. In photoelastic experiments, the birefringent material is used as a thin film coated on the sample surface in undeformed configuration. Various interference mechanisms (Cloud, 2009; Fourney, 1968; Post et al., 1994) are used for photoelasticity depending on the optics setup. In some experimental setup, grating patterns are used as the surface coating layer (Post, 1972). The surface coating layer deforms together with the sample surface under mechanical loads. The local deformation gradient is calculated from the periodic fringes produced by interference between two polarized light beams with some phase lag (Fourney, 1968). The photoelastic characterization provides a linear map from the 2D surface domain to in-plane deformation field in $\mathbb{R}^2$,as illustrated in Fig. 1 (b). The DInM uses the birefringent material as a functional module – Nomarski prism – in an imaging system, not attached to the sample surface. The Nomarski prism does not only produce a constant phase lag but also shears one polarized light beam relative to the other by a very small angle usually in μrads. On the sample surface, the sheared light for imaging illuminates a surface area where the information of local out-of-plane variation is captured by the DInC image. This is illustrated in Fig. 2 (a), without loss of generality, we can set the coordinate system $x_1 - x_2 - x_3$where $x_1 - x_2$spans the sample surface with x_1 axis

[1] We use DInC for differential interference contrast to distinguish from DIC for digital image correlation.

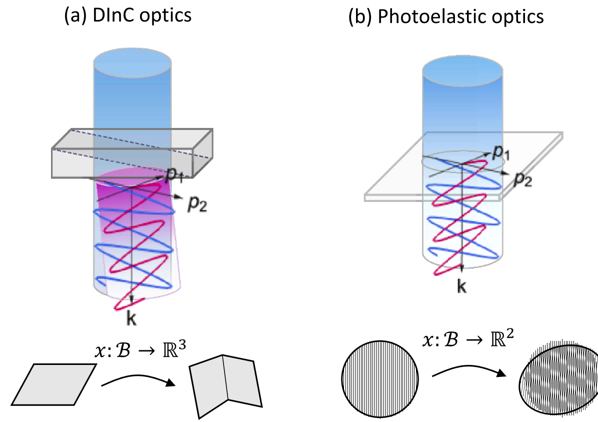

Fig. 1. (a) Light passing a Nomarski prism consisting of two birefringent crystal wedges used to generate a beam-shear between orthogonally polarized light rays, which characterizes a topographic map from a 2D domain to $\mathbb{R}^3$. **(b)**Light passing a birefringent film used for a common photoelasticity measurement. From the undeformed configuration to deformed configuration, periodic fringes form due to the interference between the orthogonally polarized light rays having a phase lag.

aligned with the beam-shear direction, and x_3 denotes the out-of-plane direction aligned with light propagation. Let $\mathcal{B}$be the field of view exposed by the light with a sufficiently small beam-shear angle, the DInM gives a pixelated gray-scale image, *e.g.* Fig. 2(b). For any pixel $(x_1, x_2) \in \mathcal{B}$, the phase lag ϕ is related to the local variation of x_3 in Fig. 2(c) by

$$\phi(x_1, x_2) = \frac{2\pi}{\lambda}[x_3(x_1 + s, x_2) - x_3(x_1, x_2)] \tag{2}$$

where the value $s \in (0, \infty)$ is the magnitude of the beam-shear vector (Zeng et al., 2019). The intensity field $\mathcal{I}$of the DInM image depends on the phase lags generated during both illumination and imaging paths, calculated as

$$\mathcal{I}(x_1, x_2) = \mathcal{I}_0(x_1, x_2)\sin^2(\phi(x_1, x_2) + \phi_0) + \mathcal{I}_s. \tag{3}$$

Here $\mathcal{I}_0$,ϕ_0 and $\mathcal{I}_s$are the optical parameters that have been calibrated before characterization. The parameters $\mathcal{I}_0$and $\mathcal{I}_s$represent the intensity fields of the reference illumination path without Nomarski prism and the residual intensity caused by the stray light. Their calibration procedures have been introduced in reference Zeng et al. (2019). The parameter ϕ_0 is the phase lag generated by the functional optics in the light path. There is one more essential parameter for this characterization, that is the beam-shear vector $\mathbf{s} = (s, 0)$written in $x_1 - x_2 - x_3$basis. Not only it determines the accuracy of surface topography, it also plays an important role in lateral resolution of our method, which means that the lateral resolution of DInM depends on two factors: light wavelength and beam-shear vector.

The single beam-shear DInM with application to experimental mechanics has several limitations. The reported DInM method does not trace the surface deformation with respect to the reference configuration. That is, all measures are under Euler description. Even in

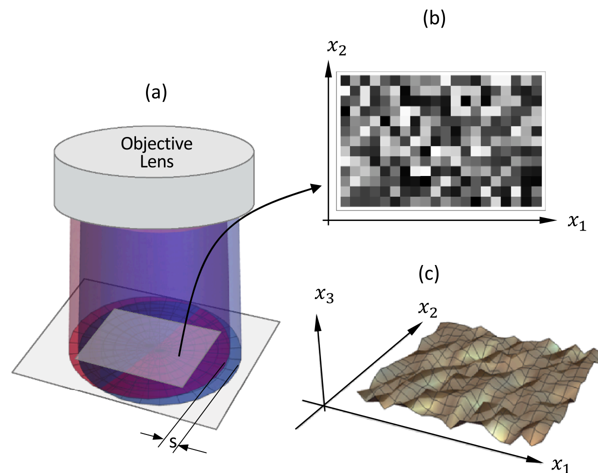

Fig. 2. Schematic of the image domain exposed by a beam-shear light. **(a)** Sheared light illuminates the sample surface within the field of view shown as **(b)** the pixelated gray-scale image consisting of **(c)** the 3D surface topography information.

some cases, the spatial form of deformation is the goal of characterization, the single beam-shear feature fails to give a full tensor measure of ($\partial x_3/\partial x_1$, $\partial x_3/\partial x_2$). All commercially available DInC microscopes do not provide the accurate value of the beam-shear vector, that is neither magnitude nor direction information are available. Last but not least, all commercial microscopes use halogen light source, which is highly incoherent. This will cause large errors in the calculation of phase using the equations (2) and (3). In order to turn the idea of DInC to a true experimental mechanics method DInM, we need to underlie a set of equations for mechanics characterization, completely re-design the light path to achieve the full tensor field measurement, setup the accurate calibration standards and implement the control and post-image processing algorithms.

3. Dual beam-shear differential interference microscopy

As demonstrated in the single beam-shear mode, we successfully characterized the surface topography for a laminated twinning structure using a commercial Nikon Ni-U reflected light DInC microscope (Zeng et al., 2019). This section will extend the theory for the DInM characterization using a dual beam-shear mode. The overall design of the light path is shown in Fig. 3(a). We use the LED light (ThorLabs M470L3) to replace the halogen source, which is sufficiently coherent for our design and less self-diffractive than the laser source. Fig. 3 (b) shows the energy spectrum of our LED source with the expectation value of wavelength $\lambda = 472.11$nm. The dual beam-shear mode is implemented by two liquid crystal retarders (LC1 and LC2) and two Nomarski prisms.

The illumination path starts from a blue collimated LED light, which passes the polarizer (P1) and becomes a linearly polarized light. The linearly polarized light is reflected by a non-polarizing beamsplitter cube (BS) toward the dual beam-shear module: LC1 - Prism1 - LC2 - Prism2. After passing through the dual beam-shear module, the sheared light is focused at the back-focal plane of the objective lens. The depth of focus is in range of several microns to tens of microns depending on the type of objective lens. Note that this value does not solely determine the upper bound of the components $\partial x_3/\partial X_i$ ($i = 1, 2$) because the magnitudes of the beam-shear vectors also play a role. The imaging light path is accounted as the reflected light by the sample surface, which follows the same route back and passes the beamsplitter cube (BS) and an analyzer (P2), finally reaches the camera for imaging. In our design, both speed and image quality are equally important. Integrated with the budget consideration, we choose the Zyla sCMOS 5.5 PLUS camera with speed of 100 fps and dynamic range 33,000.

The dual beam-shear mode is implemented by a set of optics: LC1 - Prism1 - LC2 - Prism2. The working mechanism is illustrated in Fig. 3(c). We use the liquid crystal to manipulate the phase lag between two polarizations without inducing spatial shears. The

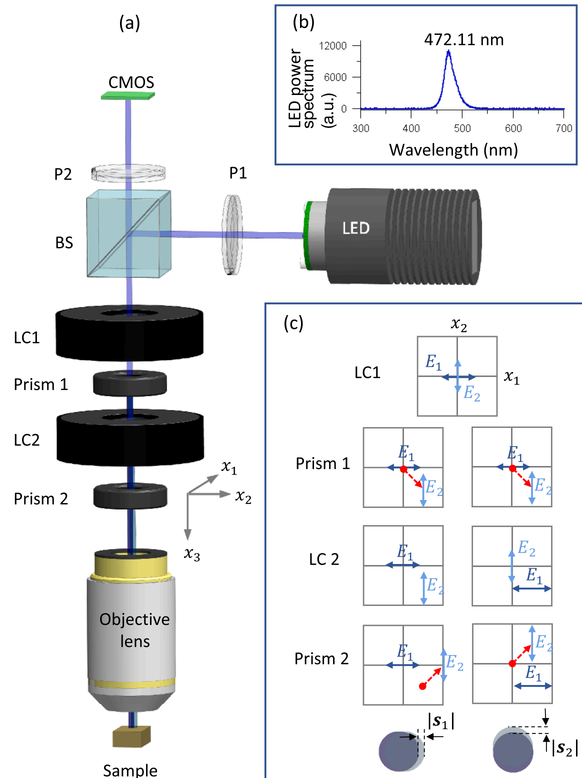

Fig. 3. The principle of dual beam-shear differential interference microscopy: light path and beam-shear mechanisms. (a) The overall illumination and imaging light path and corresponding optical modules. (b) The spectrum of the LED light source used for DInM. (c) The illustration of the transverse field at different optical stages with respect to the two beam-shear modes.

principle of phase-tuning is similar to that of the photoelasticity measurement illustrated in Fig. 1 (b). That is the propagation of electromagnetic waves is perpendicular to two principal directions of the crystal permittivity tensor while the phase of one polarization is retarded to the other because of the crystal anisotropy. Here we use two identical liquid crystal retarders (LCC1221-A from Thorlabs) for adding an arbitrary small phase lag (LC1) and swapping polarization components between x_1 and x_2 directions (LC2). The mathematical derivations for implementing the dual beam-shear function are concluded in Appendix. At each of the beam-shear modes, the shear vectors of the polarized light are

$$\begin{aligned} &\mathrm{BS1}:(s,0),\\ &\mathrm{BS2}:(0,\tilde{s}) \end{aligned} \tag{4}$$

The scalars s and $\tilde{s}$are the magnitudes of the shear distances caused by the Nomarski Prism 1 and 2. In our experimental setting, $s \approx \tilde{s}$. In Section 4, we determine their precise values using the localization method (Chiu et al., 2019).

After the light reaches the sample surface and is reflected back passing through the same light path, the analyzer P2 is used to superimpose the two polarizations and then the CMOS camera captures the differential interference image for the intensity field $|\mathbf{E}|^2$ for each of the beam-shear modes respectively. For post processing, the effective intensity profiles are calculated as

$$\mathrm{BS1}:\widehat{\mathcal{I}}_1 = \mathcal{I}_1 - \mathcal{I}_s = \mathcal{I}_0 \sin^2\left([s]\frac{\partial x_3}{\partial x_1} + \epsilon + \delta_1\right) \tag{B1}$$

$$\mathrm{BS2}:\widehat{\mathcal{I}}_2 = \mathcal{I}_2 - \mathcal{I}_s = \mathcal{I}_0 \sin^2\left([\tilde{s}]\frac{\partial x_3}{\partial x_2} + \epsilon + \delta_2\right) \tag{B2}$$

where $[s] = \frac{2\pi s}{\lambda}$, $[\tilde{s}] = \frac{2\pi \tilde{s}}{\lambda}$are the dimensionless optical constants, $\mathcal{I}_{1,2}$are the intensity fields measured at the CMOS camera by our system, $\mathcal{I}_0$is the reference intensity field without the dual beam-shear module, $\mathcal{I}_s$is the environmental intensity caused by stray light, ϵ is the phase induced by prisms and $\delta_{1,2}$ are the total relative retardances caused by the two LC retarders. The local differential components $\left(\frac{\partial x_3}{\partial x_1}, \frac{\partial x_3}{\partial x_2}\right)$are the decoupled variables of (B1) and (B2). Except the reference intensity $\mathcal{I}_0$,the rest constants and coefficients in (B1) and (B2) can be determined and calibrated prior to the measurement.

To solve for the surface differential variables from (B1) and (B2), we have to take 2 frames in each of the beam-shear modes, *i.e.* 4 frames in total. In the ith beam-shear mode, $i = 1,2$,we acquire the frames $\widehat{\mathcal{I}}_i$and $\widehat{\mathcal{I}}_i'$at two retardances δ_i and δ_i'. The surface differential component $x_{3,i}$for $i = 1,2$can be calculated from

$$\frac{\widehat{\mathcal{I}}_i}{\widehat{\mathcal{I}}_i'} = \frac{\sin^2([s]x_{3,i} + \epsilon + \delta_i)}{\sin^2([s]x_{3,i} + \epsilon + \delta_i')}. \tag{5}$$

We only consider the surface differential component in the range shown in Fig. 4 within which the sinusoidal function is non-negative for both frames. The range of measurement for $x_{3,i}$ is from $\frac{-(\epsilon+\delta_i)}{[s]}$ to $\frac{\pi-\epsilon-\delta_i'}{[s]}$. Using our current optical parameters, the measurable range presented as the surface inclined angle are $[-5^\circ, 7^\circ]$. The spatial scale of common surface reliefs and deformed microstructures are usually in the scale of one to hundreds of microns. If we consider a lateral 100 microns microstructure, the surface descent/elevation would be measured up to 12% out-of-plane strain, which has been sufficient for most solid mechanics problems in mesoscale. If a larger measurable range of out-of-plane deformation is requested, we can couple 2 or 3 periods of the sinusoidal function. For simplicity, here we only derive the differential variable $x_{3,i}$within the designed range. Let $\phi_i = \epsilon + \delta_i$and $\Delta\delta_i = \delta_i' - \delta_i$,equation (5) becomes

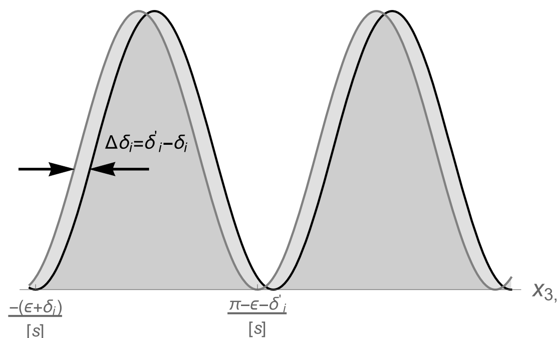

Fig. 4. The range of measurement for the surface differential component $x_{3,i}$.

$$\left(\cos\Delta\delta_i\sqrt{\frac{\widehat{\mathcal{I}}_i}{\widehat{\mathcal{I}}_i'}}-1\right)\sin\left([s]x_{3,i}+\phi_i\right)=-\sin\Delta\delta_i\sqrt{\frac{\widehat{\mathcal{I}}_i}{\widehat{\mathcal{I}}_i'}}\cos\left([s]x_{3,i}+\phi_i\right). \tag{6}$$

We choose a small enough $\Delta\delta_i$ between the two frames such that the measurable region is sufficiently large (Fig. 4), then

$$x_{3,i}=\begin{cases}\dfrac{\pi/2-\phi_i}{[s]}, & \cos\Delta\delta_i\sqrt{\dfrac{\widehat{\mathcal{I}}_i}{\widehat{\mathcal{I}}_i'}}=1\\ \dfrac{1}{[s]}\arctan\left(-\dfrac{\sin\Delta\delta_i\sqrt{\dfrac{\widehat{\mathcal{I}}_i}{\widehat{\mathcal{I}}_i'}}}{\cos\Delta\delta_i\sqrt{\dfrac{\widehat{\mathcal{I}}_i}{\widehat{\mathcal{I}}_i'}}-1}\right)-\dfrac{\phi_i}{[s]}, & \cos\Delta\delta_i\sqrt{\dfrac{\widehat{\mathcal{I}}_i}{\widehat{\mathcal{I}}_i'}}<1\\ \dfrac{1}{[s]}\arctan\left(-\dfrac{\sin\Delta\delta_i\sqrt{\dfrac{\widehat{\mathcal{I}}_i}{\widehat{\mathcal{I}}_i'}}}{\cos\Delta\delta_i\sqrt{\dfrac{\widehat{\mathcal{I}}_i}{\widehat{\mathcal{I}}_i'}}-1}\right)+\dfrac{\pi-\phi_i}{[s]}, & \text{else.}\end{cases} \tag{7}$$

The expression for the out-of-plane differential variables given by (7) is analytical. In principle, if our camera and the response of our optics are sufficiently fast, we can capture the quantitative evolution of the surface deformation from the reference configuration in real time. We can characterize the Lagrangian components $\left(\frac{\partial x_1}{\partial X_1},\frac{\partial x_2}{\partial X_2}\right)$ by local digital image correlation (DIC) in post image processing. This will be illustrated in Section 5. The out-of-plane Lagrangian components of deformation gradients for $I=1,2$ are calculated as

$$x_{3,I}=\frac{\partial x_3}{\partial x_i}\frac{\partial x_i}{\partial X_I}=\frac{\partial x_3}{\partial X_I}. \tag{8}$$

Practically, there exist artificial singularities in the DInC image from the system fluctuations. In addition, surface defects of the specimen introduce non-transforming discontinuities in the image as well. These facts make the measured gradient field incompatible, which causes the imaging domain not integratable, thus the three-dimensional surface topography can not be attained directly from the measured gradient field. Let $\nabla x_3(\mathbf{x})=x_{3,i}\in\mathbb{R}^2$ for all $\mathbf{x}\in\mathcal{B}$ represent the measured gradient field by dual beam-shear DInM. There exists a compatible gradient field close to ∇x_3, which is curl-free and

$$\min_{\nabla\times\xi=0}\ \|\ \xi-\nabla x_3(\mathbf{x})\ \|,\ \text{for all}\ \mathbf{x}\in\mathcal{B}. \tag{9}$$

Here $\|\cdot\|$ is the vector L2 norm. The norm in (9) is a quadratic function of $\xi\in\mathbb{R}^2$ under the linear constraint $\nabla\times\xi=0$. Therefore, for any given 1 million meshgrid domain $\mathcal{B}$, (9) always has a global minimum. Let $\nabla\overline{x}_3\in\mathbb{R}^2$ be the minimizer of (9), the integration

$$x_3(x_1,x_2)=\int_{\mathcal{C}}\nabla\overline{x}_3\ d\ell \tag{10}$$

is unique independent of the integration path $\mathcal{C}\subset\mathcal{B}$. We set $x_3(0,0)=0$ as the initial condition, and calculate the relative surface height profile by direct integration of (10). In contrast to many scanning based surface probes such as atomic force microscope and laser surface profiler, the gradient field of our approach is exact, but the deformation field (or displacement field) is derived. The 3-dimensional topography given by our experiment is verified by the thin-film buckling experiment in Section 5.1.

4. Parameters calibration and system synchronization

The accuracy of the out-of-plane deformation gradient components strongly depend on the optical parameters. However, there have not been any standard calibration procedures proposed for the DInM method. This section will introduce our calibrations for 1) optical constants $[s]$ and $[\tilde{s}]$ for both beam-shear modes, 2) liquid crystal retardence 4) bias phase of the Nomarski prism and 5) stray light intensity.

4.1. Optical constants

We use a spectrometer (Ocean Optics USB4000) to calibrate the wavelength of our blue LED light (ThorLabs M470L3) with a nominal wavelength marked as 470nm. The collimated LED light directly shines on the sensor of the spectrometer, with which we plot the power spectrum in Fig. 3(b). The profile of the spectrum is fitted by a Gaussian function, whose expectation value $\lambda = 472.11$nm is used as the calibrated wavelength in our measurement.

The beam-shear angles in each of the shear modes are calibrated by the localization analysis of the transverse polarizations in Fourier space. The detailed methodology have been reported in reference Chiu et al. (2019). The inset of Fig. 5 cites the underlying principle of the method, which uses a half-wave plate (HWP) to rotate the linear polarization of the incident light before reaching the prism. In our system, we treat the LC1 - Prism 1 - LC2 - Prism 2 as an integrated module. The mean shear angle is calculated as $\alpha = \frac{\Delta}{f}$where Δ is the mean separation of the two polarizations in the Fourier plane and $f = 15$mm is the focal length for the calibration device. For the system built in Fig. 3(a), the beam-shear angles are $\alpha_1 = 58.8 \pm 1.733\mu$rads for BS1, $\alpha_2 = 59.1 \pm 1.667\mu$rads for BS2.

The objective lens used for this system is 10X Nikon CFI60 TU Plan Epi ELWD Infinity Corrected with focal length $f_{\mathrm{DInM}} = 20$mm. The magnitudes of the two beam-shears are $|s| = \alpha_1 f_{\mathrm{DInM}} = 1176$nm and $|\tilde{s}| = \alpha_2 f_{\mathrm{DInM}} = 1182$nm. Substituting the wavelength, the dimensionless optical constants of our system are

$$[s] = \frac{2\pi s}{\lambda} = 15.6544, \quad [\tilde{s}] = \frac{2\pi\tilde{s}}{\lambda} = 15.7308. \tag{11}$$

4.2. Liquid crystal retardance

We use an individual optical system in Fig. 6(a) to calibrate the relation between the retardance $\phi_{\mathrm{LC}}$and the applied DC voltage V. We use the same LED source as the incoming light. It passes a linear polarizer (P1) with polarization axis along x_2, then the filtered electric field with components $(0, E)$ passes through the tested LC with its fast axis aligned along the 45° counter clockwise from x_1. By (A.4), the outgoing transverse electric field is

$$\mathbf{E} = \frac{E}{2} e^{ik_1 x_3} \begin{bmatrix} 1 - e^{i\phi_{\mathrm{LC}}} \\ 1 + e^{i\phi_{\mathrm{LC}}} \end{bmatrix}. \tag{12}$$

The outgoing beam gets filtered by another polarizer (P2) with polarization axis along x_1. Finally its transverse component $\frac{E}{2}e^{ik_1x_3}(1 - e^{i\phi_{\mathrm{LC}}})$is captured at the power meter (Thorlabs PM200) as

$$\mathcal{I}_{\mathrm{LC}} = \frac{|E|^2}{2}(1 - \cos\phi_{\mathrm{LC}}). \tag{13}$$

The relation between intensity and the retardance is plotted in Fig. 6(b). Since the retardance $\phi_{\mathrm{LC}}$is a function of the applied electric field, we smoothly tune the DC voltage from 0 to 10V on the LC retarder and collect the corresponding intensity values as shown in Fig. 6 (c). By equation (13), the characterized intensity - voltage relationship can be converted to the retardance - voltage relationship

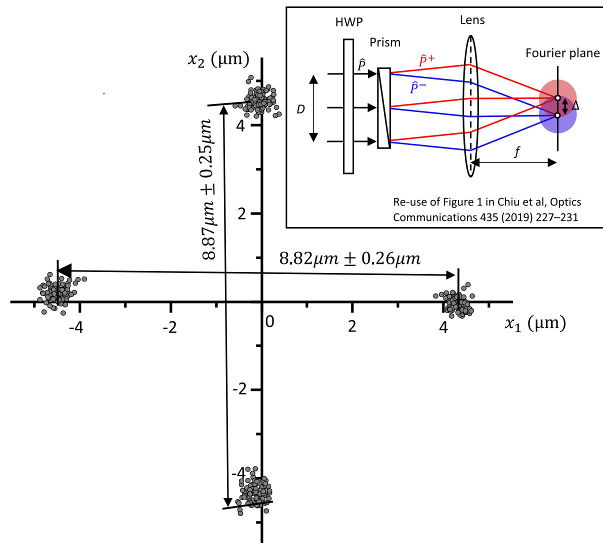

Fig. 5. Localization analysis of the transverse polarizations in Fourier space for beam-shear angle calibration.

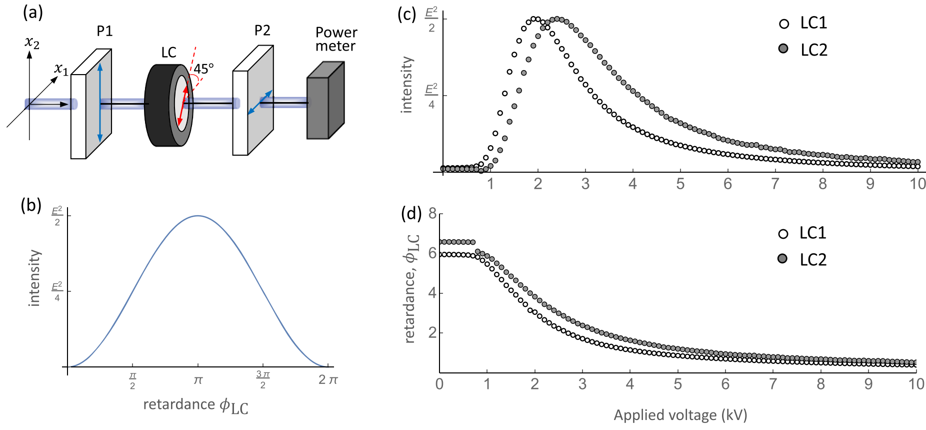

Fig. 6. Optics for calibration of liquid crystal retardance. (a) Experiment setup, (b) Theoretical intensity calculated by (13). At the power meter, the calibration results of our LC1 and LC2: (c) Voltage dependent intensity spectrum measured by the Power meter, (d) Calculated retardance - voltage relation.

as shown in Fig. 6 (d). We conduct this calibration independently for the two LC retarders used in our dual beam-shear DInM system, by which we can precisely assign a π retardance to LC2, and any designate retardance with the voltage control.

4.3. *Other system parameters*

The stray light intensity and the constant phase lag caused by two in-series prisms are calibrated every time before conducting the dual beam-shear DInM characterization. We use a flat Si wafer as the standard sample under DInM, the captured intensity can be expressed as

$$\mathcal{I}_i = \mathcal{I}_0 \sin^2(\phi_i) + \mathcal{I}_s, \quad i = 1, 2 \tag{14}$$

where the surface differential term $x_{3,i} = 0$for the flat standard sample for both beam-shear modes, and ϕ_i characterizes the total biased phase induced by all relevant optics such as retarders and prisms. As indicated in Fig. 6(d), by tuning voltage from 0 to 10 V, we can change the retardance of nearly 2π which covers more than one period of sin $^2(\cdot)$. The stray light profile for ith beam-shear mode is

$$\mathcal{I}_{s_i} = \min_{\phi_i \in [0, 2\pi]} \mathcal{I}_i. \tag{15}$$

In principle, the stray light intensity is independent of the beam-shear modes, therefore the intensity profiles $\mathcal{I}_{s_1}$ and $\mathcal{I}_{s_2}$should be the same up to statistical errors in different beam-shear modes. If the chosen standard sample is not perfectly flat, such deviations may increase. In practice, we calibrate it independently for both beam-shear modes. The initial reference intensity profile can be calculated by $\mathcal{I}_0 = \max_{\phi_i} \mathcal{I}_i - \mathcal{I}_{s_i}$. But it may change during the surface deformation, we do not use it directly to compute the surface differential variables.

In the real experimental settings, the total bias phase ϕ_i consists of two parts: the phase lag caused by the prisms ϵ and the retardance δ_i under specific applied electric field. Here δ_i is readily from Fig. 6(d) for both beam-shear modes. The phase lag by prism is independent of the beam-shear mode, thus we use BS1 to calculate it as

$$\epsilon = \arcsin < \sqrt{\frac{\mathcal{I}_1 - \mathcal{I}_0}{\mathcal{I}_{s_1}}} > -\delta_1(V_0) \tag{16}$$

where V_0 is the assigned voltage for driving δ_1 retardence in LC1 and $< \cdot >$ is the average value of the normalized intensity over all image pixels. For our system $\epsilon = 0.57335$.

4.4. *Implementation for dynamic measurement*

For any characterization of homogenous deformations, it is necessary to capture an image sequence showing the continuous change of surface topographies from a reference configuration. That is, we need to implement a dynamic measurement using dual beam-shear modes during loadings/unloadings. The frame rate of the camera is 100 fps under standard global shutter mode for a full 4M pixels image. This speed is set without consideration of data transferring time. In order to improve the speed of video recording, we will capture 1M pixels by the rolling shutter mode, which reduces the exposure time to 5ms. Together with the data transfer, it takes 9ms for each of the image frame. However this is not the effective speed of our system because we need to acquire two image frames for each of the beam-shear modes in series. Here we define an *effective frame* as the bundle of 2(BS1) + 2(BS2) images. We also need to

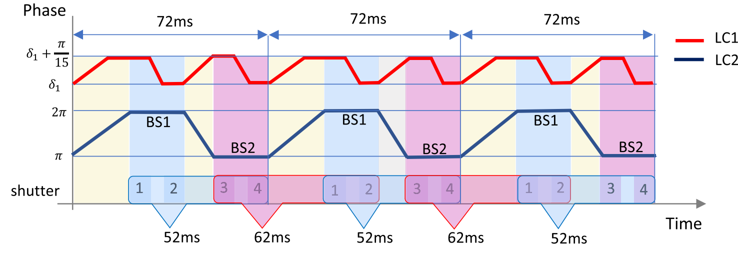

Fig. 7. Algorithm of synchronization for camera and LC retarders.

synchronize the data transferring time with the control of retarders to minimize the cost of dummy time.

Fig. 7 underlies the algorithm of the synchronization between the camera shutter and two retarders. The retardance of LC1 is set to switch between δ_1 and $\delta_1 + \frac{\pi}{15}$, while the retardance of LC2 switches between 2π[2] and π. The ramping time of the LC retarders are asymmetric during rising and falling periods. According to Fig. 6(d), the retardance decreases as the applied voltage increasing and the phase tuning is more sensitive at a higher applied voltage. For LC1, the rising / falling time from a small δ_1 (*i.e.* high voltage phase) is 10ms and 3ms respectively. For LC2, the rising / falling time is 20ms and 10ms respectively. The red / blue lines in Fig. 7 are the optimized control sequences for each of the retarders. The duration when LC2 is at 2π corresponds to the beam-shear mode 1 (BS1) marked as the blue regions, while the duration when LC2 is at π corresponds to the beam-shear mode 2 (BS2) marked as the red regions. Within each of the beam-shear modes, the first and second images are taken in series with a 3ms idle time. This idle time is synchronized with the phase falling time of LC1. As shown in Fig. 7, the neighboring effective frames share two image frames, which results in a total of five effective frames in $3 \times 72 = 216$ms, therefore the effective frame rate of our system is counted as $1000/(216/5) = 23$fps.

5. Experimental demonstration of dual beam-shear DInM

The first prototype of the dual beam-shear DInM is built in the reflected imaging mode for opaque materials. The Hong Kong Light Innovative Technology Ltd. helped us to upgrade our system to a state-of-the-art dual beam-shear (BS) DInM with an additional transmitted image function for transparent materials. All theoretical calculations as well as the parameter calibrations are implemented and integrated into a software written in LabView. This section uses two examples to demonstrate the quantitative measurement of surface deformation gradient by the dual beam-shear DInM.

5.1. Silicon microribbon buckling

We use the reflected light dual beam-shear DInM to characterize the wavy profile of bucked Si microribbons on a PDMS elastomer substrate. As a system verification, we conduct a quantitative comparison for the selected surface area using the atomic force microscopy.

The free-standing silicon microribbon with dimension $2000\mu m \times 40\mu m \times 0.35\mu m$ in Fig. 8(a) was fabricated on a single crystal Si wafer based on the micro-processes introduced in reference Jiang et al. (2007). We choose the PDMS elastomer with 0.5% prestrain (*i.e.* greater than the critical prestrain for inducing buckling (Huang et al., 2005)) to transfer the silicon microribbon from the substrate as shown in Fig. 8. The chemical property of the PDMS can be manipulated by UV/ozone so that the Si ribbon is strongly adhesive to it during the transfer process (Jiang et al., 2007). After transferring, the PDMS is released gradually, and the Si microribbon start buckling as shown in Fig. 8.

The post-buckling surface topography of the Si microribbon is characterized by our system in Fig. 9 (a) $x_{3,1} = \frac{\partial x_3}{\partial x_1}$ and (b) $x_{3,2} = \frac{\partial x_3}{\partial x_2}$, in which the labeled location A-B is also measured by atomic force microscopy (AFM). The gradient component $x_{3,1}$ is mostly uniform, while $x_{3,2}$ is periodic. It reveals that the buckling direction is closely aligned with the BS2 direction. By (9) and (10), we construct the 3-dimensional topography showing the wavy surface, which agrees with the AFM measurement for the same region, shown in Fig. 9 (c). More quantitative verification is conducted by comparing the periodicity and amplitude of the buckled profile along x_2 axis. We calculate the mean value of x_3 over x_1 axis for both the re-constructed data from DInM and the data from AFM, which is plotted in Fig. 9 (d). The periodicity matches remarkably well. The x_3 profiles given by DInM and AFM agree with each other with the maximum deviation about 200nm at $x_2 = 40\mu m$. This deviation might be caused by the sample handling and traveling between different testing systems. This experiment shows that the spatial gradient and topography characterization by our new method is feasible.

[2] Because the absolute zero retardance is unachievable within the tuning voltage range at [0, 10*V*].

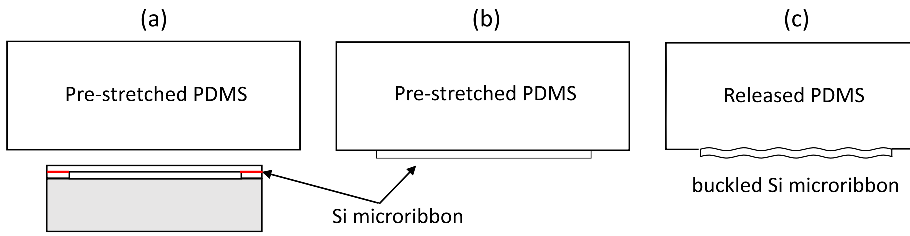

Fig. 8. Illustration of fabrication, transfer and buckling processes for Si microribbon on the PDMS pre-stretched elastomer.

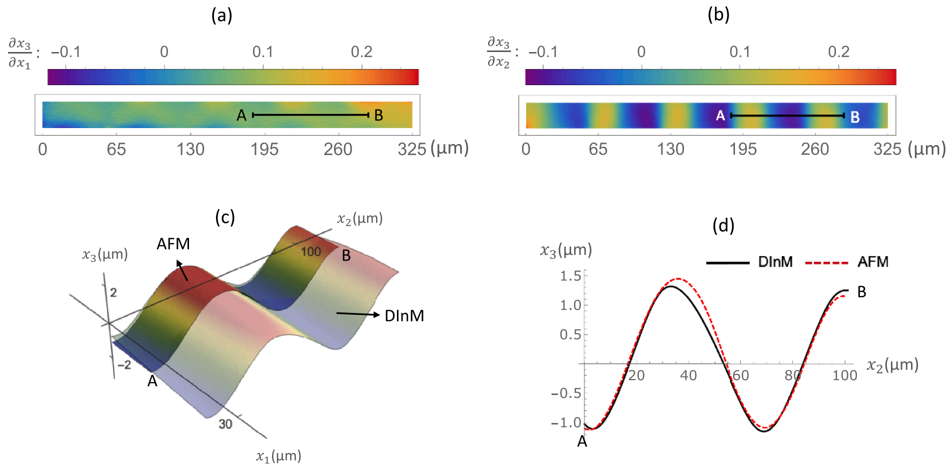

Fig. 9. (a)-(b) The measured out-of-plane gradient component $\frac{\partial x_3}{\partial x_1}$ and $\frac{\partial x_3}{\partial x_2}$. Location A – B is selected to be characterized by atomic force microscopy (AFM). (c) The 3-dimensional surface topography comparison between our system and AFM with (d) the mean $x_3$profiles over x_1 direction for DInM (black) and AFM (red dashed) respectively. (For interpretation of the references to colour in this figure legend, the reader is referred to the web version of this article.)

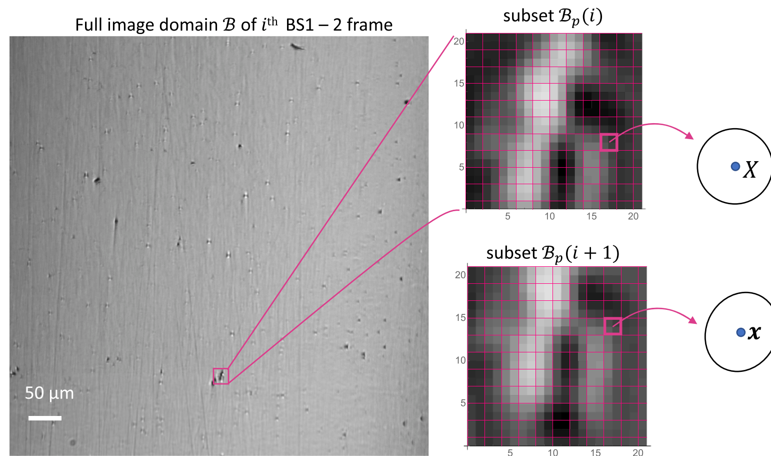

Fig. 10. Scheme of digital image correlation between neighboring image frames.

5.2. Stress-induced phase transformation of Nickel - Titanium alloy

We demonstrate the stress-induced phase transformation of a polycrystalline shape memory alloy Nickel - Titanium under uniaxial tension. Utilizing both digital image correlation and DInM (Fig. 10 and Fig. 11), the evolution of 3D surface topography is reconstructed from the measurement of the instant full-field deformation gradient tensor. Simultaneously, the corresponding stress-strain behavior was characterized by a custom-made uniaxial loading device in Fig. 11 (a). The time-dependent local deformation is captured dynamically in the loading/unloading process. The testing sample is the polycrystalline 50.8 at. % Ni-49.2 at. % Ti from

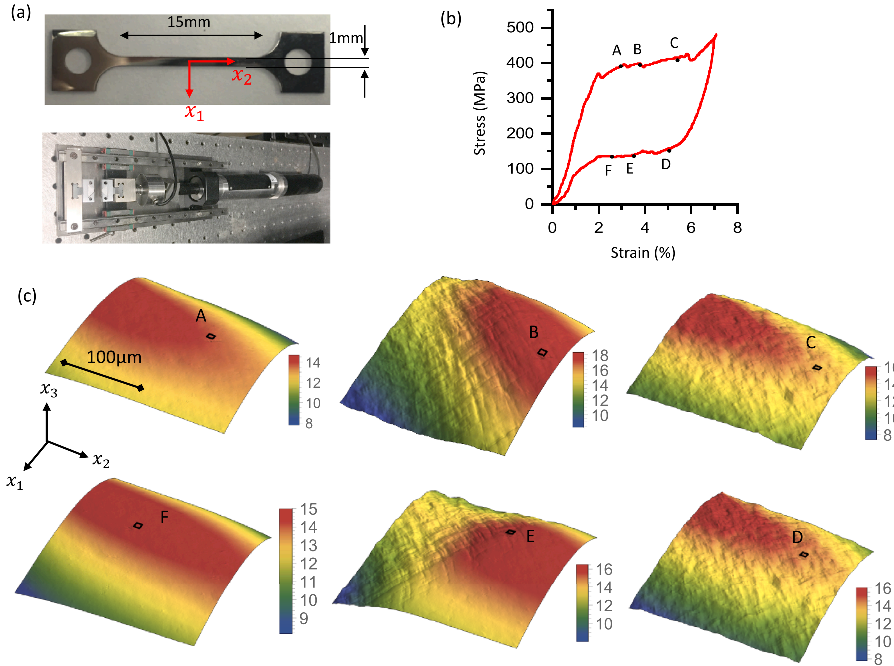

Fig. 11. (a) Geometry of the testing sample and the uniaxial loading cell for tensile test. The tensile direction is aligned with the beam-shear x_2 axis. (b) The true stress - strain curve marked by A, B, C, D, E, F stages corresponding to (c) the 3D surface topographies. The corresponding tracking zone is marked as the black square. The color bar quantifies the x_3 profile in the unit of μm. (For interpretation of the references to colour in this figure legend, the reader is referred to the web version of this article.)

Johnson Matthey Incorporation (USA) cut in a dog-bone shape of dimension 20mm × 1mm × 0.38 mm, which is in austenite at room temperature.

We use the Ncorr open-source 2D Digital Image Correlation Matlab Software (Blaber et al., 2015) to track a subset of the image between neighboring DInM frames. There are four image frames in every effective frame, two for the BS1 mode and two for the BS2 mode. In our analysis, we use the second image frame of BS1 mode as the input for the digital image correlation calculation, *e.g.* we choose a 20 × 20 pixels subset $\mathcal{B}_p \subset \mathcal{B}$of the i^{th}frame showing a non-transforming surface defect in Fig. 10. We assume that there exists a homogeneous linear transformation $\mathbf{F} : \mathbf{X} \to \mathbb{R}^2$for every $\mathbf{X} \in \mathcal{B}_p(i)$. We also assume that the intersection of the mapping $\mathbf{F}(\mathcal{B}_p(i))$and the subset $\mathcal{B}_p(i+1)$in the $(i+1)^{\text{th}}$frame is non-empty. The refined DIC solution $\mathbf{u} = (u_1, u_2)$is used to calculate the deformation gradient for all meshing centers $\mathbf{X} \in \mathcal{B}_p(i)$as

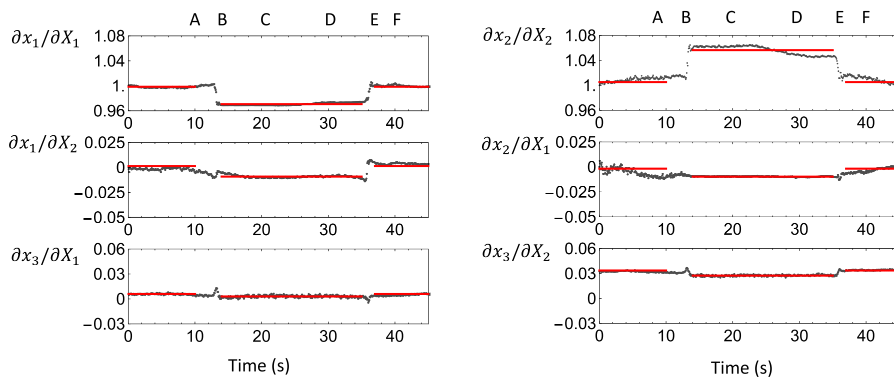

Fig. 12. The evolution of full-field deformation gradient components for a specific surface point. Red horizontal line denotes the mean value of $\partial x_i/\partial X_J$ within austenite and martensite phases respectively.

$$\begin{bmatrix} \frac{\partial x_1}{\partial X_1} & \frac{\partial x_1}{\partial X_2} \\ \frac{\partial x_2}{\partial X_1} & \frac{\partial x_2}{\partial X_2} \end{bmatrix} = \arg\min_{\mathbf{F}\in\mathbb{R}^{2\times2}} \sum_{\mathcal{B}_p(i)} \| (\mathbf{F}-\mathbf{I})\mathbf{X}-\mathbf{u} \|^2, \tag{17}$$

where $\|\cdot\|$ is the Euclidean norm of $\mathbb{R}^2$. Using the diagonal components of (17), the Lagrangian component of deformation gradient are computed by equation (8).

In DInM experiment, the tensile direction is aligned with BS2 axis (*i.e.* x_2 axis) under the uniaxial loading. The field of view of our microscope is about 300μm wide, set near the middle part of the dog-bone specimen. The synchronized presentation of the full-field deformation gradient is available in the supplementary video (titled SI_DInM_NiTi) for the surface tracking point. The evolution of 3D surface topography upon loading/unloading is shown in Fig. 11 (c) corresponding to the stress-strain curve in Fig. 11 (b). We select six DInM effective frames A, B, C, D, E, F from the reversible superelastic plateau to reveal the evolution of austenite and martensite during phase transformation, which is calculated by (10). The tracking zone given by digital image correlation is marked as the black square in each of the selected frames. Upon the uniaxial tension, the austenite start deforming elastically (frame A). When the applied stress reaches the critical value (about 400MPa), the stress-induced phase transformation occurs and the martensite phase nucleates and grows. Frames B and E capture the austenite/martensite interfaces for the forward and reverse transformation respectively, which show Lüders-like morphology similar to the reported martensite microstructure at phase front (Brinson et al., 2004; Feng and Sun, 2006; Tan et al., 2004; Zheng et al., 2016). The austenite/martensite interface propagates in different orientations for the forward and reverse transformations. They differ from the tensile direction about 45° from opposite sides. Limited by the field of view, our experiment does not fully cover the Lüders band structure. Frames C and D show the martensite morphology fully transformed from austenite.

By tracking a specific surface sub-region shown as the black square in Fig. 11, the full-field gradient tensor is characterized in Fig. 12. The stretching components $\partial x_i/\partial X_I$ dominate the states of interface distortion between two phases. The shear deformation including in-plane and out-of-plane shears is subtle. The average transformation strain calculated as

$$\langle S\rangle = \left(\sum_{i=1,2,3}\sum_{I=1,2}\left(\left\langle\frac{\partial x_i}{\partial X_I}\right\rangle_M - \left\langle\frac{\partial x_i}{\partial X_I}\right\rangle_A\right)^2\right)^{\frac{1}{2}}, \tag{18}$$

is used to quantify the transformation tensile strain, in which $<\cdot>_{A,M}$ denotes the mean value within the austenite (A) and martensite (M) respectively. Labeled as the red horizontal lines in Fig. 11, the averaged deformation gradient of austenite is

$$\left\langle\frac{\partial x_i}{\partial X_J}\right\rangle_A = \begin{bmatrix} 0.99856 & 0.00126 \\ -0.00167 & 1.00529 \\ 0.00585 & 0.03366 \end{bmatrix},$$

while the averaged deformation gradient of martensite is

$$\left\langle\frac{\partial x_i}{\partial X_J}\right\rangle_M = \begin{bmatrix} 0.97067 & -0.00916 \\ -0.00967 & 1.05646 \\ 0.00302 & 0.02754 \end{bmatrix}.$$

Direct calculation by (18) givens $\langle S\rangle = 0.06011$that agrees with the transformation strain characterized in the stress-strain curve in Fig. 11(b).

6. Discussion and conclusion

As demonstrated in the two experiments, our method is suitable to quantify the surface reliefs during the dynamic loading process in micron to sub-millimeter scales. Integrated with the theories of continuum mechanics, this micromechanics system provides 4D structure-property characterization for the deformable materials.

As the rapid development of state-of-the-art structural probes, the experimental mechanics have advanced excessively. By synchrotron X-ray diffraction microscopy, the grain structures as well as the localized deformation can be in-situ quantified, *e.g.* in strained NiTi wire (Feng and Sun, 2006; Sedmák et al., 2016) and in polycrystalline CuAuZn alloy (Chen et al., 2016). Thanks to the advanced fabrication techniques, the speckle patterns can be made in nanoscale, which enables the digital image correlation under high-resolution electron microscope (Kimiecik et al., 2016). Together with the automatic stitching algorithm by machine learning, it is now possible to resolve the twinning inside a sub-micron grain while mapping the millimeter size grain structure of martensite by digital image correlation *e.g.* in NiTi shape memory alloy (Polatidis et al., 2020) and Mg alloy (Chen et al., 2018). In addition, there are many high-quality works related to in situ observation of microstructure evolution and structural quantification (Brinson et al., 2004; Chen et al., 2016; Soejima et al., 2016).

The dual beam-shear DInM introduced in this paper can be seen as a hardware extension for digital image correlation to cover the mechanics characterization at micro to meso scale. It is also a stand-alone instrument, which directly provides the spatial deformations under dynamic loading conditions. For the phase transforming materials, it can provide a quantitative measure of deformation of a propagating interface. The existing in-situ quantitative microscopes including scanning electron microscopy and transmission electron

microscopy hardly capture the moving interface, and lack the ability to quantify the out-of-plane deformation gradient directly. In our experiment, the distortion can be captured by continuously tracing a specific surface location while the phase front passing through. From Fig. 12, the deformation gradient at time $t_B = 13.25$sec corresponds to the interface between austenite and martensite, which is evaluated as

$$S(t_B) = \frac{\partial x_i(t_B)}{\partial X_I} = \begin{bmatrix} 0.97206 & -0.00611 \\ -0.00843 & 1.04262 \\ 0.01234 & 0.03439 \end{bmatrix}. \tag{19}$$

The relative distortions between interface and austenite/martensite is $\epsilon_A = S(t_B) - \langle S \rangle_A = 0.0473$and $\epsilon_M = S(t_B) - \langle S \rangle_M = 0.01838$respectively.

In summary, this paper conclusively introduces a new experimental mechanics characterization method: dual beam-shear differential interference microscopy. The underlying principle is to precisely quantify the local differential variations of surface by the pair of spatially sheared light beams with orthogonal transverse polarizations. In order to characterize the full-field deformation gradient tensor, we design an optical microscopy, named DInM, that can capture the two dimensional surface differential variations ($x_{3,1}$, $x_{3,2}$) sequentially during the homogeneous deformation process. We justified the mathematical models and corresponding calibrations for all optical parts. Finally, we use our first prototype to successfully characterize the mechanical behaviors of 1) the buckling of Si microribbon and 2) the tensile induced martensitic phase transformation in the Nickel – Titanium alloy.

Declaration of Competing Interest

The authors declare that they have no known competing financial interests or personal relationships that could have appeared to influence the work reported in this paper.

Acknowledgement

Z. Z., C. Z., M. K. and X. C. thank the financial support of the HK Research Grants Council under the Granted projects 16207017, 16201118 and 16201019. Z. Z. and S.D. acknowledges support from Light Innovation Technology Ltd through a research contract with Hong Kong University of Science and Technology (HKUST) R and D Corporation Ltd (Project Code 16171510), and support from HKUST Office of the Vice-President for Research and Development (Project No. VPRGO12SC02 and IEG18SC01). The authors would like to acknowledge the Nanosystem Fabrication Facility (NFF) of HKUST for fabrication of the devices.

Appendix A. Derivation of dual beam-shear function

This section provides the detailed derivation for the dual beam-shear function of DInC that is implemented by two liquid crystal linear retarders. The incident light is assumed to be coherent with the linear polarization. The electric field in the liquid crystal medium should satisfy the Helmholtz wave equation

$$(\nabla^2 + \mu\boldsymbol{\epsilon})\mathbf{E} = 0, \tag{A.1}$$

where $\mu \in \mathbb{R}$is the permeability and $\boldsymbol{\epsilon} \in \mathbb{R}^2$is the permittivity tensor. Here we assume that the liquid crystal medium is isotropic in magnetization but anisotropic in polarization.

For LC1, the fast and slow axes are aligned with x_1 and x_2 directions,

$$\boldsymbol{\epsilon}_{\mathrm{LC1}} = \begin{bmatrix} \epsilon_1 & 0 \\ 0 & \epsilon_2 \end{bmatrix}, \tag{A.2}$$

where ϵ_1 and ϵ_2 are relative permittivity corresponding to the axes x_1 and x_2, respectively. For LC2, the fast and slow axes are oriented 45° counterclockwise from x_1, x_2 directions,

$$\boldsymbol{\epsilon}_{\mathrm{LC2}} = \frac{1}{2}\begin{bmatrix} \epsilon_1 + \epsilon_2 & \epsilon_1 - \epsilon_2 \\ \epsilon_1 - \epsilon_2 & \epsilon_1 + \epsilon_2 \end{bmatrix}. \tag{A.3}$$

Substituting the permittivity tensors given by (A.2) and (A.3) into equation (A.1) respectively, we get the transverse wave functions

$$\mathbf{E}(x_3) = \begin{cases} \begin{bmatrix} A_1 e^{ik_1 x_3} \\ A_2 e^{ik_2 x_3} \end{bmatrix} e^{-i\omega t} & \text{in LC1}, \\ \begin{bmatrix} A_1' e^{ik_1 x_3} + A_2' e^{ik_2 x_3} \\ A_1' e^{ik_1 x_3} - A_2' e^{ik_2 x_3} \end{bmatrix} e^{-i\omega t} & \text{in LC2}, \end{cases} \tag{A.4}$$

where the wavenumbers $k_1 = k\sqrt{\epsilon_1/\epsilon_0}$and $k_2 = k\sqrt{\epsilon_2/\epsilon_0}$with $k_1 > k_2$. The constants A_1, A_2, $A_1'$and $A_2'$are determined by the boundary

conditions. At the boundary between the vacuum and LC1, $x_3 = x_3^*$,

$$\mathbf{E}(x_3^*) = \begin{bmatrix} E_1 \\ E_2 \end{bmatrix} e^{i(kx_3^* - \omega t)} \text{ for } E_1, E_2 \in \mathbb{R}, \tag{A.5}$$

with the vacuum wavenumber $k = \frac{2\pi}{\lambda}$along x_3 direction, and $\omega = k/\sqrt{\mu\epsilon_0}$where ϵ_0 is the vacuum permittivity constant. This gives the constants $A_1 = E_1 e^{i(k-k_1)x_3^*}$and $A_2 = E_2 e^{i(k-k_2)x_3^*}$. After the light travels through LC1 with thickness ℓ, at $x_3 = x_3^* + \ell$,

$$\mathbf{E}(x^* + \ell) = \begin{bmatrix} E_1 e^{i(k_1\ell + kx_3^*)} \\ E_2 e^{i(k_2\ell + kx_3^*)} \end{bmatrix} e^{-i\omega t} = \begin{bmatrix} E_1 e^{i(k_1\ell + kx_3^*)} \\ E_2 e^{i(k_1\ell + kx_3^* - \phi_{LC})} \end{bmatrix} e^{-i\omega t}. \tag{A.6}$$

The phase of the slow axis falls behind relative to that of the fast axis by $\phi_{LC} = (k_1 - k_2)\ell$. The quantity $\phi_{LC} \in [0, 2\pi)$is defined as the retardance of the liquid crystal retarder depending on the crystal anisotropy, which can be precisely tuned by applying the DC voltage in a timely manner, usually less than 20ms. This is calibrated experimentally in next section (Fig. 6). Since then, the electric field follows the vacuum propagation as

$$\mathbf{E}(x_3) = \begin{bmatrix} E_1' \\ E_2' \end{bmatrix} e^{i(kx_3 - \omega t)}, \tag{A.7}$$

where $E_1' = \overline{A_1}$and $E_2' = \overline{A_2}$are the complex conjugates of the constants A_1 and A_2 with $|E_1'| = E_1$and $|E_2'| = E_2$. When the polarized light passes the first Nomarski prism, the polarization along $x_2$axis is sheared by $\mathbf{s}_1 = \frac{s}{\sqrt{2}}(-1, 1)$corresponding to the dashed red arrow depicted in Fig. 3 (c). After the Prism 1, the sheared beams reach the liquid crystal retarder LC2 at $x_3 = x_3^{**}$,by continuity, the constants $A_1'$and $A_2'$of the electric field in LC2 can be determined as $A_1' = \frac{1}{2}(E_1' + E_2')e^{i(k-k_1)x_3^{**}}$ and $A_2' = \frac{1}{2}(E_1' - E_2')e^{i(k-k_2)x_3^{**}}$.

We set the retardance $\phi_{LC}$of LC2 in two modes: $\phi_{LC} = 0$for beam-shear 1 (BS1) and $\phi_{LC} = \pi$for beam-shear 2 (BS2). For BS1, $\phi_{LC} = 0$implies no retardance between two crystal axes, *i.e.* $k_1 = k_2$. At $x_3 = x_3^{**} + \ell$,

$$\mathbf{E}|_{\phi_{LC}=0} = \begin{bmatrix} A_1' + A_2' \\ A_1' - A_2' \end{bmatrix} e^{i[k_1(x_3^{**} + \ell) - \omega t]} = e^{ik_1\ell}\left(\mathcal{E}_1(x_3^{**}, t)\begin{bmatrix} 1 \\ 1 \end{bmatrix} + \mathcal{E}_2(x_3^{**}, t)\begin{bmatrix} 1 \\ -1 \end{bmatrix}\right), \tag{A.8}$$

where $\mathcal{E}_1(x_3^{**}, t) = A_1' e^{i(k_1 x_3^{**} - \omega t)}$and $\mathcal{E}_2(x_3^{**}, t) = A_2' e^{i(k_2 x_3^{**} - \omega t)}$. It implies that the outgoing field remains the magnitudes of polarizations in x_1, $x_2$axes corresponding to the left diagram of Fig. 3 (c). For BS2, $\phi_{LC} = \pi$gives $e^{ik_1\ell} = -e^{ik_2\ell}$. At $x_3 = x_3^{**} + \ell$,the electric field in BS2 can be calculated as

$$\mathbf{E}|_{\phi_{LC}=\pi} = e^{ik_1\ell}\left(\mathcal{E}_1(x_3^{**}, t)\begin{bmatrix} 1 \\ 1 \end{bmatrix} + \mathcal{E}_2(x_3^{**}, t)\begin{bmatrix} -1 \\ 1 \end{bmatrix}\right). \tag{A.9}$$

Comparing to (A.8), the field given by the beam-shear mode 2 swaps the polarization axes between x_1 and x_2 corresponding to the right diagram in Fig. 3 (c). Then the light beams transverse the Prism 2, which is aligned orthogonally to Prism 1. The polarization in x_2 axis is sheared by $\mathbf{s}_2 = \frac{\tilde{s}}{\sqrt{2}}(1, 1)$. Since the polarization component in $x_2$has been swapped between the two beam-shear modes by LC2, the relative beam positions after the Prism 2 will be different as shown in the last row of Fig. 3(c). The Prism 1 and 2 are identical based on their commercial specifications (manufactured by United Crystals Inc.), the magnitude of the shear distance $\tilde{s} \approx s$. In order to precisely determine the parameters $\mathbf{s}_1$and $\mathbf{s}_2$, we use the nanometer localization analysis and the direct method (Chiu et al., 2019). The results are discussed in Section 4.

Supplementary material

Supplementary material associated with this article can be found, in the online version, at doi:10.1016/j.jmps.2020.104162

References

Blaber, J., Adair, B., Antoniou, A., 2015. Ncorr: open-Source 2D digitial image correlation matlab software. Exp. Mech. 55, 1105–1122.

Brinson, L.C., Schmidt, I., Lammering, R., 2004. Stress-induced transformation behavior of a polycrystalline NiTi shape memory alloy: micro and macromechanical investigations via in situ optical microscopy. J. Mech. Phys. Solids 52 (7), 1549–1571.

Chen, X., Tamura, N., MacDowell, A., James, R.D., 2016. In-situ characterization of highly reversible phase transformation by synchrotron x-ray laue microdiffraction. Appl. Phys. Lett. 108 (21), 211902.

Chen, Z., Lenthe, W., Stinville, J., Echlin, M., Pollock, T., Daly, S., 2018. High-resolution deformation mapping across large fields of view using scanning Electron microscopy and digital image correlation. Exp. Mech. 58 (9), 1407–1421.

Chiu, H.C., Zeng, Z., Zhao, L., Zhao, T., Du, S., Chen, X., 2019. Measuring optical beam shear angle of polarizing prisms beyond the diffraction limit with localization method. Opt. Commun. 435, 227–231.

Cloud, G., 2009. Optical methods in experimental mechanics. Exp. Tech. 33 (5), 13–17.

Feng, P., Sun, Q., 2006. Experimental investigation on macroscopic domain formation and evolution in polycrystalline niti microtubing under mechanical force. J. Mech. Phys. Solids 54 (8), 1568–1603.
Fourney, M.E., 1968. Application of holography to photoelasticity. Exp. Mech. 8 (1), 33–38.
Huang, Z., Hong, W., Suo, Z., 2005. Nonlinear analyses of wrinkles in a film bonded to a compliant substrate. J. Mech. Phys. Solids 53 (9), 2101–2118.
Jiang, H., Khang, D.-Y., Song, J., Sun, Y., Huang, Y., Rogers, J.A., 2007. Finite deformation mechanics in buckled thin films on compliant supports. Proc. Natl. Acad. Sci. 104 (40), 15607–15612.
Kimiecik, M., Jones, J.W., Daly, S., 2016. The effect of microstructure on stress-induced martensitic transformation under cyclic loading in the SMA nickel-Titanium. J. Mech. Phys. Solids 89, 16.
Nguyen, T.H., Kandel, M.E., Rubessa, M., Wheeler, M.B., Popescu, G., 2017. Gradient light interference microscopy for 3D imaging of unlabeled specimens. Nat. Commun. 8.
Nomarski, G., 1952. Interferential polarizing device for study of phase object. US Patent 2924142.
Peters, W., Ranson, W., 1982. Digital imaging techniques in experimental stress analysis. Opt. Eng. 21 (3), 213427.
Polatidis, E., Smid, M., Kubena, I., Hsu, W.-N., Laplanche, G., Van Swygenhoven, H., 2020. Deformation mechanisms in a superelastic niti alloy: an in-situ high resolution digital image correlation study. Mater. Des. 108622.
Post, D., 1972. Holography and interferometry in photoelasticity. Exp. Mech. 12 (3), 113–123.
Post, D., Han, B., Ifju, P., 1994. Moiré Interferometry. High Sensitivity Moiré. Springer, pp. 135–226.
Sedmák, P., Pilch, J., Heller, L., Kopeček, J., Wright, J., Sedlák, P., Frost, M., Šittner, P., 2016. Grain-resolved analysis of localized deformation in nickel-titanium wire under tensile load. Science 353 (6299), 559–562.
Shribak, M., Inoué, S., 2006. Orientation-independent differential interference contrast microscopy. Appl. Opt. 45 (3), 460.
Smith, F. H., 1952. Interference microscope. US Patent 2601175.
Soejima, Y., Motomura, S., Mitsuhara, M., Inamura, T., Nishida, M., 2016. In situ scanning electron microscopy study of the thermoelastic martensitic transformation in ti–ni shape memory alloy. Acta Mater. 103, 352–360.
Sutton, M., Wolters, W., Peters, W., Ranson, W., McNeill, S., 1983. Determination of displacements using an improved digital correlation method. Image Vis. Comput. 1 (3), 133.
Sutton, M.A., Orteu, J.J., Schreire, H., 2009. Image Correlation for Shape, Motion and Deformation Measurements. Springer US.
Tan, G., Liu, Y., Sittner, P., Saunders, M., 2004. Lüders-like deformation associated with stress-induced martensitic transformation in NiTi. Scr. Mater. 50 (2), 193–198.
Zeng, Z., Zhang, C., Du, S., Chen, X., 2019. Quantitative surface topography of martensitic microstructure by differential interference contrast microscopy. J. Mech. Phys. Solids 124, 102–104.
Zheng, L., He, Y., Moumni, Z., 2016. Lüders-like band front motion and fatigue life of pseudoelastic polycrystalline NiTi shape memory alloy. Scr. Mater. 123, 46–50.